Research Article

Electron-irradiation-facilitated production of chemically homogenized nanotwins in nanolaminated carbides

Hui Zhang[a,b,*], Qianqian Jin[c], Tao Hu[d,*], Xiaochun Liu[e], Zezhong Zhang[f], Chunfeng Hu[g], Yanchun Zhou[h,*], Yu Han[i], Xiaohui Wang[j]

[a]*Electron Microscopy Center, South China University of Technology, Guangzhou 510640, China*
[b]*School of Emergent Soft Matter, South China University of Technology, Guangzhou 510640, China*
[c]*Center for the Structure of Advanced Matter, School of Electronic Engineering, Guangxi University of Science and Technology, Liuzhou 545006, China*
[d]*Institute of Materials Science and Devices, School of Materials Science and Engineering, Suzhou University of Science and Technology, Suzhou 215009, China*
[e]*Institute of Metals, Changsha University of Science & Technology, Changsha 410004, China*
[f]*Electron Microscopy for Materials Research (EMAT), University of Antwerp, Antwerp 2020, Belgium*
[g]*Key Laboratory of Advanced Technologies of Materials, Ministry of Education, School of Materials Science and Engineering, Southwest Jiaotong University, Chengdu 610031, China*
[h]*School of Materials Science & Engineering, Zhengzhou University, Zhengzhou 450001, China*
[i]*Advanced Membranes and Porous Materials Center, Physical Sciences and Engineering Division, King Abdullah University of Science and Technology, Thuwal 23955-6900, Saudi Arabia*
[j]*Shenyang National Laboratory for Materials Science, Institute of Metal Research, Chinese Academy of Sciences, Shenyang 110016, China*

Abstract: Twin boundaries have been exploited to stabilize ultrafine grains and improve mechanical properties of nanomaterials. The production of the twin boundaries and nanotwins is however prohibitively challenging in carbide ceramics. Using a scanning transmission electron microscope as a unique platform for atomic-scale structure engineering, we demonstrate that twin platelets could be produced in carbides by engineering antisite defects. The antisite defects at metal sites in various layered ternary carbides are collectively and controllably generated, and the metal elements are homogenized by electron irradiation, which transforms a twin-like lamellae into nanotwin platelets. Accompanying chemical homogenization, α-Ti_3AlC_2 transforms to unconventional β-Ti_3AlC_2. The chemical homogeneity and the width of the twin platelets can be tuned by dose and energy of bombarding electrons. Chemically homogenized nanotwins can boost hardness by ~45%. Our results provide a new way to produce ultrathin (< 5 nm) nanotwin platelets in scientifically and technologically important carbide materials and showcase feasibility of defect engineering by an angstrom-sized electron probe.

* Corresponding authors.

E-mail: H. Zhang, hui.materials.zhang@gmail.com;

     T. Hu, thu@usts.edu.cn;

     Y. Zhou, yczhou@alum.imr.ac.cn

1 Introduction

Nanotwinned structures are energetically more stable than normal nanograins with comparable grain sizes as excess energy of a coherent twin boundary is roughly ten times lower than normal grain boundaries [1]. Nanotwinning has thus been used to produce stable ultrafine grains (< 5 nm) in metals, e.g., Cu [2] and Ti [3] alloys, and ceramics, e.g., diamonds [4] and cubic BN [5]. The latter generally requires extreme environments such as high pressures and high temperatures due to strong covalent bonds. Interestingly, an atomically thin twin-like lamellae naturally exists in ternary layered carbide ceramics, $M_{n+1}AC_n$ phases, which have the merits of both metals and ceramics and hold promise for the applications in high-temperature foil bearings, heating elements, electrical contacts, coatings on nuclear materials, etc. [6,7]. In these unique structures, A (A-group elements, mainly Al) layers structurally act as mirror planes of the $M_{n+1}C_n$ slabs [8] (Fig. 1(a)), where M is the transition metal element. Metallic M–A bonding in the $M_{n+1}AC_n$ phases is significantly weaker than ionic and covalent M–C bonding [9]. The twin-like interfaces, therefore, have no strengthening or hardening effect in the $M_{n+1}AC_n$ phases, yet are Achilles' heel of these structures, where deformation and delamination occur first [10,11].

It has been expected that the twin-like interfaces could be used to boost mechanical properties if we can find a way to diminish the chemical anisotropy near the interface. There are two possible routes to achieve this. One may remove the A-layers from the structure by chemical etching or heat treatment. The former results in MXenes [12] and weaker structures because of the intercalation of atoms like O, F, H, or even molecules. The latter method can produce twins, but the process is uncontrollable (Fig. S1 in the Electronic Supplementary Material (ESM)). Another way is to chemically homogenize M and A without destroying mirrored structures. Heat treatment has been used to tune the distribution of constituent elements in twins [13], but is inapplicable for the $M_{n+1}AC_n$ phases because of phase decompositions [14]. We thus turned to engineering the antisite defects with the irradiation of energetic particles.

In the $M_{n+1}AC_n$ phases, MA (M at A sites) and AM (A at M sites) antisite defects could form with the bombardment of the energetic particles [15,16] with low radiation fluence (~0.2 dpa) due to their relatively low formation energy (E_f = 2–3 eV for Ti_3AlC_2 [7]) compared to other point-defect pairs (6–8 eV). The accumulation of the antisite defects could lead to the transformation of hexagonal $M_{n+1}AC_n$ to face-centered-cubic $(M_{n+1}A)C_n$ with large amounts of nanotwins [17]. However, due to large beam size and poor controllability of beam position, the most used heavy-ion irradiation is infeasible to spatially engineer the defects at the nanometer or smaller scale, which requires atomic-scale atom manipulation. With remarkable improvements in spatial resolution [18] and electron-probe controllability [19], a scanning transmission electron microscope becomes a new platform to manipulate atoms [20–23], cations [24], and vacancies [25], trigger phase transformations [26], and induce the movement of grain [27] and phase [28] boundaries. Here, we demonstrate that angstrom-sized electron probes can work as an effective stimulator for the solid-state chemical homogenization in various $M_{n+1}AC_n$ phases to produce chemically homogenized twins.

2 Exprimental

2.1 Sample preparation and transmission electron microscopy (TEM) observation

Four MAX phases were used in this study, i.e., Nb_2SC, Ti_2AlC, Ti_3AlC_2, and Nb_4AlC_3. They were synthesized by reactive hot processing, as reported in Refs. [29–31]. For (scanning) transmission electron microscopy ((S)TEM) observations, electron transparent specimens were prepared by ion milling. Most (S)TEM characterizations were performed on a microscope (Themis Z, FEI) equipped with double aberration correctors. The convergence semi-angle (α) used in this study was 21 mrad. High-angle annular dark-field (HAADF)-STEM images were recorded with a collection semi-angle of 65 mrad. An atomic-scale elemental mapping was performed on a transmission electron microscope

(JEM-ARM200F, JEOL) with an energy-dispersive X-ray (EDX) spectrometer (0.96 sr). To estimate the electron dose (D, in e$^-$/Å^2), the probe current (x, in pA) was calibrated with a Faraday cup. The electron dose was calculated by $D = 6.242 \dfrac{xt}{(\Delta d)^2}$, where t and Δd are the dwell time on each pixel in μs and the pixel size in Å, respectively. Four-dimensional (4D) STEM datasets were recorded on an electron microscopy pixel array detector (EMPAD) [32]. The camera length was chosen to ensure that the maximum collection semi-angle was roughly three times α (21 mrad). Given long t (= 1 ms), $x \approx 5$ pA was used to avoid sample damage. Ptychographic phase images were reconstructed by the single-side band method [33,34].

2. 2　STEM simulation

HAADF-STEM simulations were performed with quantitative STEM (QSTEM) [35], where the model was set to be ~25-nm thick based on the thickness measurement by an electron energy loss spectrum. The models were sliced into 1-Å-thick layers. The frozen phonon method was used to address thermal diffuse scattering, where the results were averaged over 30 frozen phonon configurations. The residual aberrations were measured after tuning the corrector, and an inner collection semi-angle of 65 mrad was set in the simulation. The outer detector angle was 200 mrad. Debye–Waller factors of Ti, Al, and C were 0.44, 0.075, and 0.81 Å, respectively.

To semi-quantitatively determine the amount of Ti atoms repartitioned to Al-layers in Ti$_3$AlC$_2$, a library of simulated HAADF-STEM images was established. With electron irradiation, Ti atoms in Ti-layers move into the Al-layers, and the corresponding amount of Al atoms in the Al-layers goes into the Ti-layers accordingly. As demonstrated in the ptychographic phase image, carbon can migrate to the interstitial sites between the Ti-layers and the Al-layers of the pristine structure. However, carbon atoms do not affect intensity analysis of the HAADF-STEM images due to their low atomic number (Z) compared to Ti and Al, so the redistribution of the carbon atoms was not considered in the image simulation. Six models with $x = 0$, 0.05, 0.1, 0.15, 0.2, and 0.25 for (Ti$_{1-x}$Al$_x$)$_3$(Al$_{1-3x}$Ti$_{3x}$)C$_2$ were used to establish a lookup table. The intensity ratio between the Al-layers and the Ti-layers (I_{Al}/I_{Ti}) was calculated from the simulated images and fitted with x. After that, I_{Al}/I_{Ti} for the experimental images were also calculated

and averaged among the values obtained from various atomic layers in the same irradiated region to reduce experimental errors. The concentrations of Al in the Ti-layers and Ti in the Al-layers were finally calculated using the equation of $x - I_{Ti}/I_{Al}$ established with the simulated images.

2. 3　Density functional theory (DFT) calculation

The DFT calculations were performed to model the electron beam interaction with Ti$_3$AlC$_2$. The calculations were performed with the projector-augmented wave method using the Vienna *ab initio* Simulation Package [36]. Generalized gradient approximation–Perdew–Burke–Emzerhof (GGA–PBE) type exchange-correlation functional was used for all calculations [37]. The equilibrium structure of Ti$_3$AlC$_2$ was obtained by structural optimization. Total energy and Hellmann–Feynman force acting on atoms converged to 10^{-6} eV and 0.005 eV/Å^{-1}, respectively. Monkhorst–Pack scheme k-point meshes smaller than 0.5 Å^{-1} were used for the integration in the irreducible Brillouin zone. After geometric optimization, the *ab initio* molecular dynamics was performed in NVT ensemble to obtain the displacement threshold energy (E_d) and sputtering energy (E_s). An orthogonal supercell containing 96 atoms was constructed from a hexagonal unit cell, ensuring that the simulation box is larger than 10 Å along the *a*-, *b*-, and *c*-axis to avoid image interactions. The E_d was determined by running a series of the *ab initio* molecular dynamics simulations with different initial kinetic energy. We used a time step of 1 fs and the maximum time duration up to ~2 ps to ensure that the system converges to equilibrium states. The initial kinetic energy added to the primary knock-on atom (KPA) [38] along [0001] was increased with a step of 1 eV until the atom moved out of their original sites. KPA not returned to its original position within 2 ps was regarded to be a displaced atom. The E_d is the initial kinetic energy to displace KPA. As the atoms on the surface are bonded differently from the atoms within the bulk, E_s of the atoms on the surface were also calculated. Three typical surfaces, i.e., ($11\bar{2}0$), ($10\bar{1}0$), and (0001), were modeled. The slab models used in the study were at least eight-atom-layer thick, and no obvious surface reconstructions were observed in the optimized models without any initial kinetic energy added to the constituent atoms. After structural optimization, the initial kinetic momentum was added along [0001], and E_s was determined in a way similar to E_d.

3　Results and discussion

The three-layer-thick titanium carbide lamellae in Ti_3AlC_2 are mirrored with respect to the Al-layers (Figs. 1(a) and 1(b)). Crystallographically, there are two sites for Al at the twin-like plane of the titanium carbide lamellae, which leads to two polytypes, i.e., α-Ti_3AlC_2 (Fig. 1(a)) and β-Ti_3AlC_2 (Fig. 1(b)). The latter has been assumed to exist for decades [39,40] but never conclusively confirmed in the experiments before. In the HAADF-STEM images, the contrast is in proportion to $\overline{Z^n}$ (the average of Z^n for all atoms in the column along the projection direction), where $n \approx 2$. The atomic columns with high and low intensities (Figs. 1(d) and 1(g)) are the Ti-layers and Al-layers, respectively. The comparison of atomic positions in the Al-layers and Ti-layers (the green rectangles) in the $[1\overline{2}10]$ images with the structural model (Figs. 1(a) and 1(b)) suggests that Ti_3AlC_2 in Figs. 1(d) and 1(e) take α- and β-configurations, respectively. The $[10\overline{1}0]$ images of the two polytypes (Figs. 1(g) and 1(h)) agree well with the model (Fig. 1(c)). We found that the intensity of the Al-layers increases with the accumulation of electron doses along the two-zone axes (Figs. 1(e), 1(f), 1(h), and 1(i) and Videos S1 and S2 in the ESM), indicating that the certain amounts of Ti atoms run into the Al-layers. As the irradiation dose accumulates to $\sim4\times10^7$ $e^-/Å^2$, the intensity of the Al-layers reaches ~83% of the intensity of the Ti-layers (the inset in Fig. 2(a)). In Fig. 2(a), the compositions of the Ti-layers and Al-layers are estimated to be $Ti_{0.8}Al_{0.2}$ and $Al_{0.4}Ti_{0.6}$, respectively.

It is well-established that HAADF-STEM has a depth of field ($\Delta z = \lambda/\alpha^2$) [41]. Structural features within Δz are in-focus and dominate the contrast in the images. Nearly identical intensity of the Ti-layers and Al-layers in a region of ~20 nm in thickness imaged with 30 mrad ($\Delta z = 2.2$ nm), 20 mrad ($\Delta z = 4.9$ nm), and 10 mrad ($\Delta z = 19.6$ nm) (Fig. S2 in the ESM) suggest that repartitioning is not limited to the regions near the surface but throughout the sample, which is corroborated by atomic-scale mappings of Ti and Al K-signals via EDX spectroscopy (Figs. 2(b)–2(d)), where the number of the Ti atoms in the Al-layers gradually increases, while accordingly that of the Al atoms in the Al-layers decreases to the same level of the Ti-layers. As shown in Fig. S3 in the ESM, EDX simulations using quantum excitation of phonon multislice [42] suggest that the Al K-edge is more delocalized than the Ti K-edge, which seemly forms a continuous line instead of atomically resolved individual columns. Core–shell electrons of light elements are
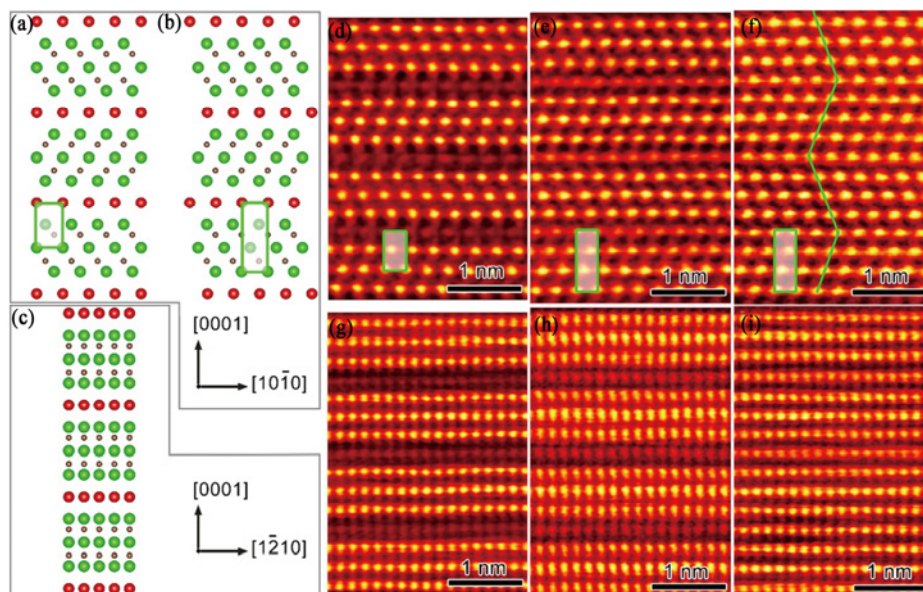

Fig. 1 Electron-irradiation-facilitated generation of carbide nanotwins. Projections of (a) α-Ti_3AlC_2 and (b) β-Ti_3AlC_2 atomic models along $[1\overline{2}10]$. (c) $[10\overline{1}0]$ projections of two polytypes are the same. Ti, Al, and C atoms are denoted by green, red, and dark-yellow balls, respectively. (d, g) HAADF-STEM images of pristine α-Ti_3AlC_2. In (e, h) and (f, i), structures have been irradiated by $\sim2\times10^7$ and $\sim4\times10^7$ $e^-/Å^2$, respectively. The green line in (f) illustrates planes corresponding to {111} of face-centered cubic structure. Twin platelets are ~1-nm thick. The rectangles in (a, b) and (d–f) highlight atoms in Ti-layers that are on the same vertical line with atoms in Al-layers. The structures in (d) and (e, f) are α- and β-polytypes, respectively.
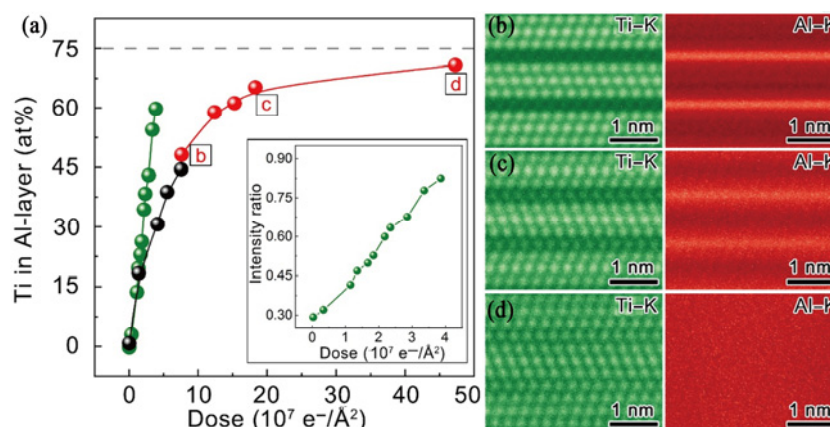
Fig. 2 Irradiation-facilitated element repartitioning in Ti_3AlC_2. (a) Concentration of Ti (at%) in Al-layers vs. electron dose. The green and black spheres are data for 300 and 200 kV, respectively. The red spheres are EDX data collected at 200 kV. The dashed line denotes concentration limit, where Ti and Al are completely homogenized. Concentrations were determined by semi-quantitative analysis of HAADF-STEM images (the green and black spheres) and EDX quantification (the red spheres). The inset shows I_{Al}/I_{Ti} in the structure irradiated by various doses. (b–d) Atomic-resolution EDX mappings corresponding to points marked in (a).

weakly bound to their nuclei, as compared to those of heavy elements. As a consequence, the light elements exhibit a rather delocalized ionization potential for X-ray generation [43]. However, the homogenization of Al is still evident in Figs. 2(b)–2(d). Irradiation-induced repartitioning also occurs in other Al-containing MAX phases, e.g., Ti_2AlC (Videos S3 and S4 in the ESM) and Nb_4AlC_3 (Fig. S4 in the ESM). It is noted that there is no noticeable repartitioning in Nb_2SC (Fig. S4 in the ESM), which might be due to the remarkably high E_f (8.6 eV) of M/A antisite defects compared to those of Al-containing MAX phases (2.0–3.5 eV) like Ti_3AlC_2, Ti_2AlC, Nb_2AlC, and Nb_4AlC_3 (Table 1). The antisite-defect E_f of Cr_2AlC (1.96 eV), V_2SnC (3.74 eV), and Ti_3SiC_2 (2.67 eV) are close to those of Ti_3AlC_2 and Nb_4AlC_3, and thus we anticipate that chemical repartitioning could also be observed in these MAX phases. The repartitioning is readily controllable by the electron dose and energy of the impinging electrons (Fig. 2(a)). The number of the Ti

atoms is redistributed into the Al-layers, monotonically scaling with dose accumulation. The trends revealed by EDX quantification and semi-quantitative analysis of the HAADF-STEM images are pretty consistent, and monitoring the intensity change in the HAADF-STEM images could directly give a fairly good estimate of the process in practice.

The elemental process of repartitioning is knock-on of Ti, Al, and C atoms. The *ab initio* molecular dynamics simulation suggests that Ti/Al and C atoms in defect-free Ti_3AlC_2 need ~13 and ~5 eV, respectively, to be knocked out (Fig. S5 and Video S5 in the ESM and Table 2), which could be sufficiently supplied by the energy transfer from the impinging electrons to Ti_3AlC_2 at 300 kV, where Ti, Al, and C atoms can be powered with 17.8, 31.6, and 70.9 eV, respectively, according to the calculation model proposed in Ref. [44]. In a real electron-atom interaction, the atoms on the surface are the easiest and earliest to be knocked out, which is known as sputtering [44]. Depending on the surface plane, the energy needed by Ti, Al, and C to be sputtered is 2–6 eV (Table 2), which could be easily met by the energy transfer from 200 kV electrons to those atoms, the maximum of which is 11.0 eV for Ti, 19.4 eV for Al, and 43.7 eV for C. The sputtering of constituent atoms on the surface creates defects, which will significantly lower E_d of the atoms near the surface and result in a cascade effect. Therefore, Ti/Al antisite defects were observed at 200 kV (Fig. 2), despite that the maximum energy of Ti obtained from impinging electrons is slightly lower than the threshold

Table 1 E_f of M/A antisite defects

Material	E_f (eV)
Ti_2AlC	2.71
Cr_2AlC	1.96
V_2SnC	3.74
Nb_2AlC	2.49
Nb_2SC	8.58
Ti_3SiC_2	2.67
Ti_3AlC_2	2.88
Nb_4AlC_3	3.27

Table 2 E_d and E_s. Ti_{Al}, Al_{Ti}, C_i, and Al_i stand for Ti at Al sites, Al at Ti sites, interstitial C atoms, and interstitial Al atoms, respectively

	KPA	E_d and E_s (eV)	Final defect
Knock-on	Ti	37	Ti_{Al} and Al_{Ti}
	Al	29	Ti_{Al}, Al_{Ti}
	C	5	C_i
	Ti, Al, and C	13	Ti_{Al}, Al_{Ti}, and C_i
Sputtering	Ti, Al, and C on ($11\bar{2}0$)	6	C_i and Al_i
	Ti, Al, and C on ($10\bar{1}0$)	2	C_i
	Ti, Al, and C on (0001)	5	C_i

Note: As the constituent atoms were observed to migrate between basal planes, the initial momentums in the simulation were added along [0001].

calculated with the defect-free model (11.0 vs. 13.0 eV). Actually, the Ti atoms can even be knocked out at 80 kV [23]. The lower energy the incident electrons have, the less energy can be transferred to the atoms within the sample, and the fewer atoms could be powered to the energy threshold needed to move out of their original crystal sites. Therefore, it takes a higher electron dose at 200 kV (the black spheres in Fig. 2(a)) than that at

300 kV (the green spheres in Fig. 2(a)) to achieve the same level of atomic repartition. At 200 kV, the Ti atoms in the Al-layers approach the limit of 75% with a dose of $\sim 4.7 \times 10^8$ e$^-$/Å^2, where nearly complete homogenization is attained. With the complete homogenization of Ti and Al, the structure becomes nanotwins. The twin platelets are equivalent to the $\sum 3\{111\}$ twin lamellae in a face-centered cubic structure. With further irradiation, the adjacent twin platelets could be merged into a thicker one, e.g., ~ 3 nm in Fig. S6 in the ESM.

Carbon atoms are much easier to be knocked out considering the low E_d (~ 5 eV) and high kinetic energy (~ 71 eV at 300 kV) that they can get from impinging electrons. However, we were unable to see where the displaced C atoms stay in the HAADF-STEM images (Fig. 1) due to the well-known intrinsic limitation of this imaging modality. Alternatively, we turned to the 4D-STEM ptychographic phase imaging, which has remarkable light-element sensitivity [45]. The C columns are unequivocally resolved in the phase image (the black arrows in Fig. 3(a)). The remarkably inhomogeneous intensity of the C-layers marked by the
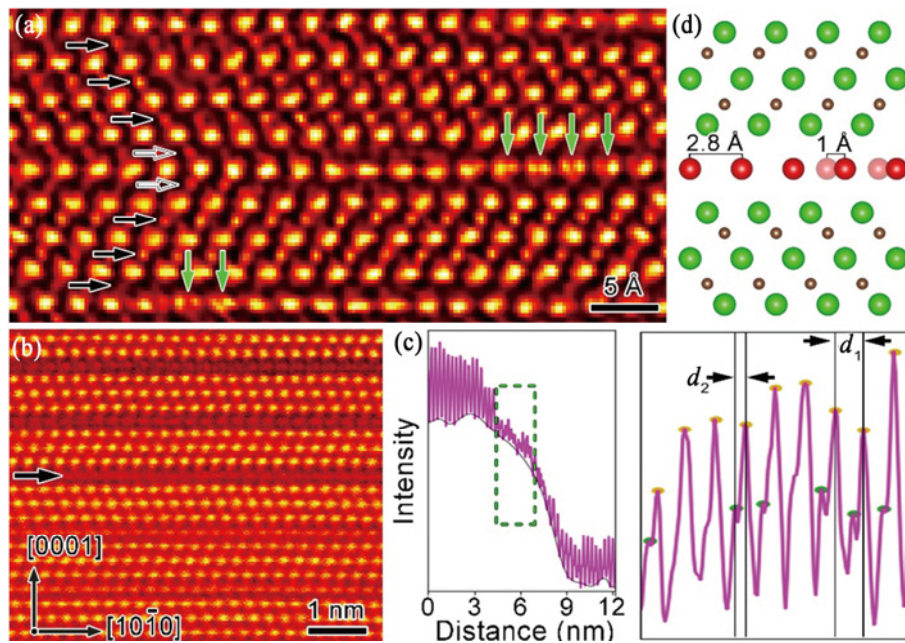

Fig. 3 Structural transition regions in irradiated Ti$_3$AlC$_2$. (a) Ptychographic phase image of formed twins. The sample was irradiated by $\sim 4 \times 10^7$ e$^-$/Å^2. The solid and hollow black arrows mark carbon columns. The green arrows highlight columns, where atomic positions of Al layers in α and β are both occupied. (b) Line-like layer marked by the black arrow near transformed Ti$_3$AlC$_2$ (the lower half). Nanotwins formed in the bottom region. (c) Intensity profile along line-like layers between pristine and transformed regions in Fig. S7 in the ESM. The green dashed rectangle region is enlarged on the right ($d_1 = 0.28$ nm and $d_2 = 0.1$ nm, where d_1 corresponds to the distance between Al columns in α- or β-polytype, and d_2 is the space of Al columns between α- and β-polytype). (d) Projection showing Al columns in α- (the red balls) and β- (the shadowed red balls) polytypes. Ti and C columns are denoted by the green and dark-yellow balls, respectively.

solid black arrows suggest that some displaced C atoms stay at the interstitial sites of carbide lamellae. More importantly, some displaced C atoms move to the space between the Al-layers and the Ti-layers (the hollow black arrows in Fig. 3(a)). Interestingly, the homogenization of C is significantly slower than those of Ti and Al, which is counterintuitive given the highly movable nature of C (Video S5 in the ESM). However, the present microstructural studies cannot provide reasonable explanations due to the lack of enough time resolution. The time resolution of the current microscope is at the scale of microseconds, which is too long to be able to reveal the dynamical repartitioning process, and the application of ultrafast cameras capable of capturing images in nanoseconds may shed insights on counterintuitive repartitioning behavior of C.

Accompanying the repartitioning of the constituent atoms, the α-polytype (Figs. 1(d) and 1(g)) transforms into the β-polytype (Figs. 1(e), 1(f), 1(h), and 1(i)). We observed that the α- and β-polytypes coexist between the nanotwins and their pristine counterparts, exhibiting line-like contrasts in the HAADF-STEM image (Fig. 3(b)). The line profile of the line-like layer (the transition region in Fig. S7 in the ESM) shows two different periodicities, i.e., $d_1 = 0.28$ nm and $d_2 = 0.1$ nm (Figs. 3(c) and 3(d)). The pairs with a 0.1-nm distance are clearly resolved in the ptychographic phase image (the green arrows in Fig. 3(a)).

The β-polytype is metastable and has never been synthesized before [7,46]. However, it gradually becomes thermodynamically more favorable than the most common α-polytype with the formation of Ti_{Al} and Al_{Ti} antisite defects (Fig. 4(a)). Specifically, the value of the energy difference between the β- and α-polytype ($E_β - E_α$) becomes negative when 32%–48% (~40% on average) Al in the Al-layers are replaced
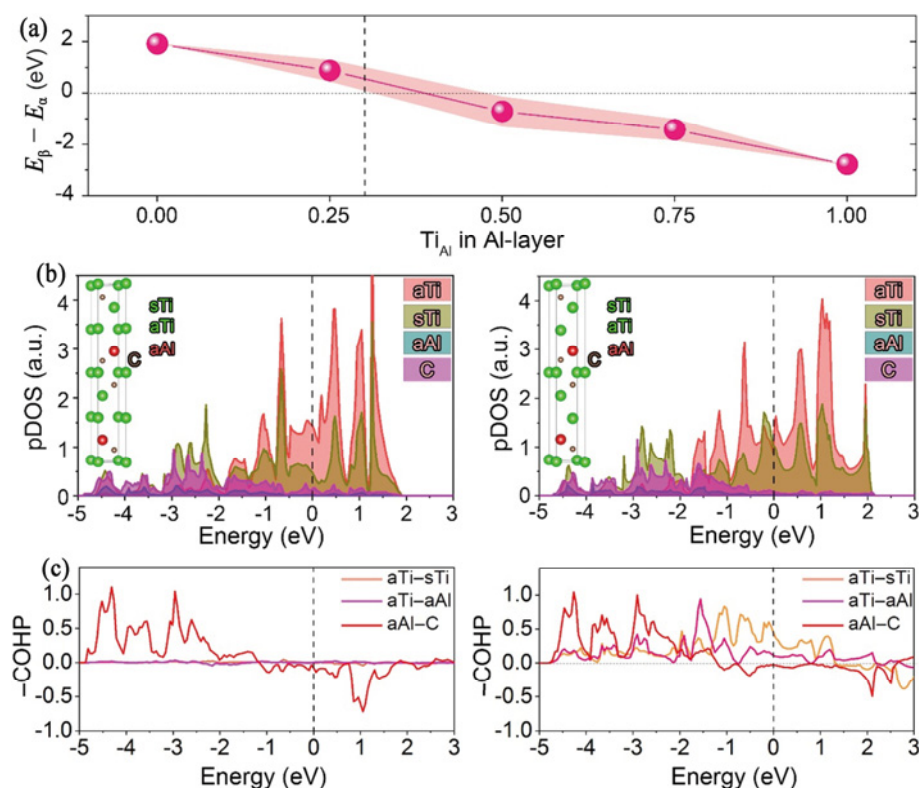

Fig. 4 Energetics and bonding analysis of polytypic transformation. (a) $E_β - E_α$ with 0%, 25%, 50%, 75%, and 100% Al in Al-layers replaced by Ti atoms near Al-layers. The shadowed region denotes the difference range obtained from calculations with multiple configurations, as shown in Figs. S8–S13 in the ESM. The red spheres are average values. The negative values mean that β is energetically favorable. (b) pDOSs of aTi 3d, sTi 3d, aAl 3p, and C 2p orbitals in α (the left panel) and β (the right panel) with Al atoms in Al-layers completely replaced by Ti atoms just below Al-layers. Ti atoms in Al-layers are denoted by aTi, while those above Al-layers are indicated by sTi. Al atoms in Ti-layers are referred to as aAl. The insets show positions of aTi, sTi, aAl, and C. (c) COHP curves of α (the left panel) and β (the right panel) for aTi and aAl and their neighboring atoms (sTi and C). E_F was set to zero. Positive, zero, and negative −COHP values signify bonding, nonbonding, and antibonding interactions, respectively. The models used for (b, c) are displayed in Fig. S14 in the ESM.

by Ti, suggesting that the α-to-β transition may occur if 32%–48% Ti_{Al} forms in the Al-layers, which is remarkably consistent with the experiments, where we observed that the β-polytype forms, when ~30% Al was replaced by Ti (Fig. 1(e)). To elucidate the stabilization mechanism of the β-polytype, we closely inspected the electron structures via the partial densities of states (pDOSs; Fig. 4(b)). In the energy range from −5 eV to Fermi energy (E_F), Ti 3d electrons are dominant compared to Al and C. For the α-polytype, PDOSs of antisite Ti (aTi) and neighboring Ti (sTi) at E_F are 1.47 and 0.46 a.u., respectively. The significant difference in PDOS between aTi and sTi suggests that breaking Ti–C bonds may render considerable amounts of 3d electrons in the α-polytype unsaturated. While in the β-polytype, PDOSs of aTi and sTi at E_F are close (0.89 a.u. vs. 0.88 a.u., respectively), and the peaks at −0.40– −0.10 eV are largely overlapped, indicating that orbital hybridization occurs between aTi and sTi, which reduces the unsaturated 3d electrons. We thus speculated that the pronounced difference in electronic structures dictates the relative stability of the α- and β-polytype. To gain more insights into this issue, bonding states of aTi, antisite Al (aAl), sTi, and C atoms were calculated via crystal orbital Hamilton population (COHP) curves [47]. As can be seen in Fig. 4(c), nonbonding states of aTi prevail in the highest occupied bands close to E_F in the α-polytype, while the β-polytype is massively characterized by aTi–sTi and aTi–aAl bonding interactions. The integrated COHP (ICOHP) of β is more negative than that of α for orbitals (Table 3), confirming stronger bonding interactions in β, which makes the β-polytype more stable.

Angstrom-sized electron probes can serve not only

as a markedly coherent "light source" for advanced real-space imaging but also as a highly controllable power source for atoms to jump out of their potential valley. Using a state-of-the-art transmission electron microscope, we homogenized M and Al elements in various $M_{n+1}AlC_n$ and produced ultrathin (< 5 nm) carbide nanotwin platelets. The homogenization process is readily controllable by the electron dose and energy. Accompanying the homogenization, the unconventional β-polytype forms in Ti_3AlC_2. More importantly, the irradiated region could dilate ~3.0% along the *c*-axis (Fig. S15 in the ESM), contract by ~0.6% along the *a*-axis, and expand by ~1.9% in volume. The slight volumetric expansion exerts compressive stress on the untransformed region. In addition, the chemical homogenization removes bonding anisotropy of Ti_3AlC_2 and turns the weak twin-like interface into strong twin boundaries of $(Ti,Al)_3C_2$. We speculate that these two factors have positive effects on mechanical properties. As a proof-of-concept study, we irradiated the Ti_3AlC_2 bulk sample (Fig. S16 in the ESM) and measured microhardness. Ti and Al were nearly completely homogenized in the ~3 nm subsurface region (Fig. S17 in the ESM), and the microhardness was improved by ~45% (Fig. 5).

Table 3   ICOHP up to Fermi level of aTi–sTi, aTi–aAl, and aAl–C bonding for α- and β-Ti_3AlC_2 with 100% Al replaced by Ti

ICOHP	α-Ti_3AlC_2	β-Ti_3AlC_2
aTi–sTi	−0.04	−1.31
aTi–aAl	−0.03	−1.21
aAl–C	−4.34	−4.48

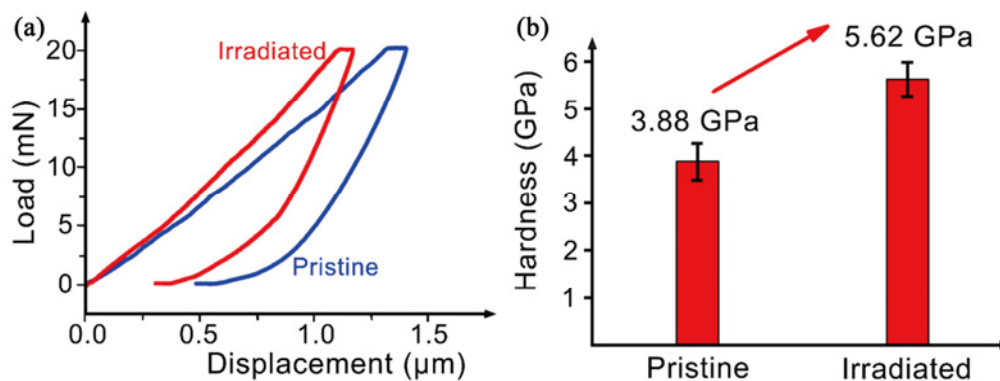Note: More negative ICOHP indicates a stronger interaction.

Fig. 5 (a) Typical load–displacement curves and (b) microhardness of pristine and irradiated regions. Hardness before and after irradiation were measured on a dynamic ultra-micro hardness tester. The maximum load, loading rate, and holding time were 20 mN, 0.8883 mN/s, and 5 s, respectively. Five spots in pristine and irradiated regions were randomly chosen for hardness measurement.

4   Conclusions

We demonstrate that the nanotwins (< 5 nm) could be produced in various $M_{n+1}AC_n$ phases (e.g., Ti_2AlC, Ti_3AlC_2, and Nb_4AlC_3) by electron irradiation, and the width of the twin platelets is tunable by manipulating the electron doses. In the most extensively investigated $M_{n+1}AC_n$ phase, Ti_3AlC_2, electron irradiation produces massive metal antisite defects in a readily controllable way. The accumulation of those antisite defects chemically homogenizes the twin-like structure and turns the twin-like interface into the twin boundaries. Using the atomic-resolution ptychography, carbon atoms were observed in the carbides for the first time, which provides direct evidence of the homogenization of the carbon atoms as electrons bombard Ti_3AlC_2. With the formation of nanotwinned platelets, the microhardness increases by ~45%. In addition, we unequivocally prove that Ti_3AlC_2 can transform from the α-polytype to the β-polytype with the irradiation of electrons. The transformation is also corroborated by the first-principles calculations. Universality and tunability of chemical repartitioning by electron irradiation provide a feasible tool for defect and crystal-structure engineering and open a huge space to produce high-performance nanotwinned transition metal carbides.

Declaration of competing interest

The authors have no competing interests to declare that are relevant to the content of this article. The author Chunfeng Hu is the Editorial Committee member of this journal. The author Yanchun Zhou is the Associate Editor of this journal.

Electronic Supplementary Material

Supplementary material is available in the online version of this article at https://doi.org/10.26599/JAC.2023.9220757.

References

[1]   Lu K. Stabilizing nanostructures in metals using grain and twin boundary architectures. *Nat Rev Mater* 2016, **1**: 16019.

[2]   Li XY, Jin ZH, Zhou X, *et al.* Constrained minimal-interface structures in polycrystalline copper with extremely fine grains. *Science* 2020, **370**: 831–836.

[3]   Zhu YM, Zhang K, Meng ZC, *et al.* Ultrastrong nanotwinned titanium alloys through additive manufacturing. *Nat Mater* 2022, **21**: 1258–1262.

[4]   Huang Q, Yu DL, Xu B, *et al.* Nanotwinned diamond with unprecedented hardness and stability. *Nature* 2014, **510**: 250–253.

[5]   Tian YJ, Xu B, Yu DL, *et al.* Ultrahard nanotwinned cubic boron nitride. *Nature* 2013, **493**: 385–388.

[6]   Barsoum MW. *MAX Phases: Properties of Machinable Ternary Carbides and Nitrides*. Weinheim, Germany: John Wiley & Sons, 2013.

[7]   Zhou AG, Liu Y, Li SB, *et al.* From structural ceramics to 2D materials with multi-applications: A review on the development from MAX phases to MXenes. *J Adv Ceram* 2021, **10**: 1194–1242.

[8]   Zhang H, Hu T, Wang XH, *et al.* Structural defects in MAX phases and their derivative MXenes: A look forward. *J Mater Sci Technol* 2020, **38**: 205–220.

[9]   Wang JY, Zhou YC. Recent progress in theoretical prediction, preparation, and characterization of layered ternary transition-metal carbides. *Annu Rev Mater Res* 2009, **39**: 415–443.

[10] Barsoum MW, Farber L, El-Raghy T. Dislocations, kink bands, and room-temperature plasticity of Ti_3SiC_2. *Metall Mater Trans A* 1999, **30**: 1727–1738.

[11] Barsoum MW, Radovic M. Elastic and mechanical properties of the MAX phases. *Annu Rev Mater Res* 2011, **41**: 195–227.

[12] Naguib M, Kurtoglu M, Presser V, *et al.* Two-dimensional nanocrystals produced by exfoliation of Ti_3AlC_2. *Adv Mater* 2011, **23**: 4248–4253.

[13] Nie JF, Zhu YM, Liu JZ, *et al.* Periodic segregation of solute atoms in fully coherent twin boundaries. *Science* 2013, **340**: 957–960.

[14] Pang WK, Low IM, O'Connor BH, *et al. In situ* diffraction study of thermal decomposition in Maxthal Ti_2AlC. *J Alloys Compd* 2011, **509**: 172–176.

[15] Wang CX, Tracy CL, Ewing RC. Radiation effects in $M_{n+1}AX_n$ phases. *Appl Phys Rev* 2020, **7**: 041311.

[16] Wang CX, Yang TF, Tracy CL, *et al.* Disorder in $M_{n+1}AX_n$ phases at the atomic scale. *Nat Commun* 2019, **10**: 622.

[17] Yang TF, Wang CX, Liu WL, *et al.* Formation of nano-twinned structure in Ti_3AlC_2 induced by ion-irradiation. *Acta Mater* 2017, **128**: 1–11.

[18] Chen Z, Jiang Y, Shao YT, *et al.* Electron ptychography achieves atomic-resolution limits set by lattice vibrations. *Science* 2021, **372**: 826–831.

[19] Sang XH, Lupini AR, Unocic RR, *et al.* Dynamic scan control in STEM: Spiral scans. *Adv Struct Chem Imaging* 2016, **2**: 1–8.

[20] Dyck O, Ziatdinov M, Lingerfelt DB, *et al.* Atom-by-atom fabrication with electron beams. *Nat Rev Mater* 2019, **4**: 497–507.

[21] Susi T, Meyer JC, Kotakoski J. Manipulating low-dimensional materials down to the level of single atoms with electron irradiation. *Ultramicroscopy* 2017, **180**: 163–172.

[22] Jesse S, He Q, Lupini AR, *et al*. Atomic-level sculpting of crystalline oxides: Toward bulk nanofabrication with single atomic plane precision. *Small* 2015, **11**: 5895–5900.

[23] Zhang H, Hu T, Sun WW, *et al*. Atomic repartition in MXenes by electron probes. *Chem Mater* 2019, **31**: 4385–4391.

[24] Yang SZ, Sun WW, Zhang YY, *et al*. Direct cation exchange in monolayer MoS_2 via recombination-enhanced migration. *Phys Rev Lett* 2019, **122**: 106101.

[25] Hopkinson DG, Zólyomi V, Rooney AP, *et al*. Formation and healing of defects in atomically thin GaSe and InSe. *ACS Nano* 2019, **13**: 5112–5123.

[26] Parajuli P, Park H, Kwon BJ, *et al*. Direct observation of electron beam-induced phase transition in $MgCrMnO_4$. *Chem Mater* 2020, **32**: 10456–10462.

[27] Wei JK, Feng B, Ishikawa R, *et al*. Direct imaging of atomistic grain boundary migration. *Nat Mater* 2021, **20**: 951–955.

[28] Lin YC, Dumcenco DO, Huang YS, *et al*. Atomic mechanism of the semiconducting-to-metallic phase transition in single-layered MoS_2. *Nat Nanotechnol* 2014, **9**: 391–396.

[29] Romero M, Huerta L, Akachi T, *et al*. X-ray photoelectron spectroscopy studies of the electronic structure of superconducting Nb_2SnC and Nb_2SC. *J Alloys Compd* 2013, **579**: 516–520.

[30] Wang XH, Zhou YC. Solid–liquid reaction synthesis of layered machinable Ti_3AlC_2 ceramic. *J Mater Chem* 2002, **12**: 455–460.

[31] Zhang H, Hu T, Wang XH, *et al*. Discovery of carbon-vacancy ordering in Nb_4AlC_{3-x} under the guidance of first-principles calculations. *Sci Rep* 2015, **5**: 14192.

[32] Tate MW, Purohit P, Chamberlain D, *et al*. High dynamic range pixel array detector for scanning transmission electron microscopy. *Microsc Microanal* 2016, **22**: 237–249.

[33] Rodenburg JM, Bates RHT. The theory of super-resolution electron microscopy via Wigner-distribution deconvolution. *Philos T R Soc A* 1992, **339**: 521–553.

[34] Pennycook TJ, Lupini AR, Yang H, *et al*. Efficient phase contrast imaging in STEM using a pixelated detector. Part 1: Experimental demonstration at atomic resolution. *Ultramicroscopy* 2015, **151**: 160–167.

[35] Koch CT. Determination of core structure periodicity and point defect density along dislocations. Ph.D. Thesis. Phoenix, USA: Arizona State University, 2002.

[36] Kresse G, Furthmüller J. Efficient iterative schemes for *ab initio* total-energy calculations using a plane-wave basis set. *Phys Rev B* 1996, **54**: 11169–11186.

[37] Perdew JP, Burke K, Ernzerhof M. Generalized gradient approximation made simple. *Phys Rev Lett* 1996, **77**: 3865–3868.

[38] Liu B, Petersen B, Zhang YW, *et al*. Layered structure induced anisotropic low-energy recoils in Ti_3SiC_2. *J Am Ceram Soc* 2016, **99**: 2693–2698.

[39] Liu XM, Le Flem M, Béchade JL, *et al*. XRD investigation of ion irradiated $Ti_3Si_{0.90}Al_{0.10}C_2$. *Nucl Instrum Meth B* 2010, **268**: 506–512.

[40] Deng TY, Sun JR, Tai PF, *et al*. Ti_3AlC_2, a candidate structural material for innovative nuclear energy system: The microstructure phase transformation and defect evolution induced by energetic heavy-ion irradiation. *Acta Mater* 2020, **189**: 188–203.

[41] Borisevich AY, Lupini AR, Pennycook SJ. Depth sectioning with the aberration-corrected scanning transmission electron microscope. *PNAS* 2006, **103**: 3044–3048.

[42] Allen LJ, D'Alfonso AJ, Findlay SD. Modelling the inelastic scattering of fast electrons. *Ultramicroscopy* 2015, **151**: 11–22.

[43] Oxley MP, Allen LJ. Atomic scattering factors for K-shell and L-shell ionization by fast electrons. *Acta Crystallogr A* 2000, **56**: 470–490.

[44] Egerton RF, McLeod R, Wang F, *et al*. Basic questions related to electron-induced sputtering in the TEM. *Ultramicroscopy* 2010, **110**: 991–997.

[45] Ophus C. Four-dimensional scanning transmission electron microscopy (4D-STEM): From scanning nanodiffraction to ptychography and beyond. *Microsc Microanal* 2019, **25**: 563–582.

[46] Wang XH, Zhou YC. Layered machinable and electrically conductive Ti_2AlC and Ti_3AlC_2 ceramics: A review. *J Mater Sci Technol* 2010, **26**: 385–416.

[47] Wuttig M, Lüsebrink D, Wamwangi D, *et al*. The role of vacancies and local distortions in the design of new phase-change materials. *Nat Mater* 2007, **6**: 122–128.